



**HAL**  
open science

# Investigation of the mechanical properties of MnSi via EBSD-nanoindentation coupling and ab-initio calculation

Mahdi Mejri, Benoît Malard, Yohann Thimont, Damien Connétable, Pascal Floquet, Raphaël Laloo, Arnaud Proietti, Claude Estournès

► **To cite this version:**

Mahdi Mejri, Benoît Malard, Yohann Thimont, Damien Connétable, Pascal Floquet, et al.. Investigation of the mechanical properties of MnSi via EBSD-nanoindentation coupling and ab-initio calculation. *Journal of Alloys and Compounds*, 2022, 900, pp.163458. 10.1016/j.jallcom.2021.163458 . hal-03597715

**HAL Id: hal-03597715**

**<https://hal.science/hal-03597715v1>**

Submitted on 4 Mar 2022

**HAL** is a multi-disciplinary open access archive for the deposit and dissemination of scientific research documents, whether they are published or not. The documents may come from teaching and research institutions in France or abroad, or from public or private research centers.

L'archive ouverte pluridisciplinaire **HAL**, est destinée au dépôt et à la diffusion de documents scientifiques de niveau recherche, publiés ou non, émanant des établissements d'enseignement et de recherche français ou étrangers, des laboratoires publics ou privés.










## Open Archive Toulouse Archive Ouverte (OATAO)

OATAO is an open access repository that collects the work of Toulouse researchers and makes it freely available over the web where possible

This is an author's version published in: <http://oatao.univ-toulouse.fr/28775>

**Official URL:** <https://doi.org/10.1016/j.jallcom.2021.163458>

### To cite this version:

Mejri, Mahdi  and Malard, Benoît  and Thimont, Yohann  and Connétable, Damien  and Floquet, Pascal  and Laloo, Raphaël  and Proietti, Arnaud and Estournès, Claude  *Investigation of the mechanical properties of MnSi via EBSD-nanoindentation coupling and ab-initio calculation.* (2022) Journal of Alloys and Compounds, 900. 163458. ISSN 0925-8388

Any correspondence concerning this service should be sent to the repository administrator: [tech-oatao@listes-diff.inp-toulouse.fr](mailto:tech-oatao@listes-diff.inp-toulouse.fr)

# Investigation of the mechanical properties of $Mn_{15}Si_{26}$ via EBSD-nanoindentation coupling and ab-initio calculation

M. Mejri<sup>a</sup>, B. Malard<sup>b</sup>, Y. Thimont<sup>a</sup>, D. Connétable<sup>b</sup>, P. Floquet<sup>c</sup>, R. Laloo<sup>a</sup>, A. Proietti<sup>d</sup>, C. Estournès<sup>a,\*</sup>

<sup>a</sup> CRIMAT, Université de Toulouse, CNRS, Université Toulouse 3 - Paul Sabatier, 118 Route de Narbonne, 31062 Toulouse cedex 9, France

<sup>b</sup> CRIMAT, Université de Toulouse, CNRS, INP, ENSIACET - 4 allée Emile Monso BP44362, 31030 Toulouse cedex 4, France

<sup>c</sup> Laboratoire de Génie Chimique, Université de Toulouse, CNRS, INPT, UPS, Toulouse, France

<sup>d</sup> Centre de Microcaractérisation Raimond Castaing, UMS 3623, Université de Toulouse, Espace Clément Ader, 3 rue Caroline Aigle, 31400, Toulouse, France

## ARTICLE INFO

### Keywords:

High Manganese Silicide  
 $Mn_{15}Si_{26}$   
Spark Plasma Sintering  
Anisotropy  
Stiffness tensor  
Nanohardness  
Young's modulus  
Ab-initio calculation

## ABSTRACT

The goal of this study is to investigate the mechanical and elastic characteristics of the  $Mn_{15}Si_{26}$  compound via experimental nanoindentation measurements and ab-initio calculations. The mechanical properties such as Young's modulus (E) and nanohardness are important inputs for improving the design and mechanical reliability of thermoelectric modules. The high-energy X-ray diffraction pattern of  $Mn_{15}Si_{26}$  has been indexed with the Miller indices of a tetragonal crystalline structure whose cell parameters are the following:  $a = b = 5.535(3)$  Å and  $c = 65.552(4)$  Å. Nanoindentation measurements, with a Berkovich indenter tip have been performed on higher manganese silicide (HMS) compound mainly composed of  $Mn_{15}Si_{26}$  grains. For the first time ever, it has been evidenced that both elastic modulus and nanohardness of the latter varied significantly depending on their crystallographic orientations provided by electron backscatter diffraction. Nanohardness and Young's modulus along the  $\langle 001 \rangle$  orientations are higher than the  $\langle 100 \rangle$  ones. The nanohardness value of  $Mn_{15}Si_{26}$  ranges from 16 GPa to 20 GPa and the Young's modulus measured varies between 234 GPa and 300 GPa. The stiffness tensor ( $S_{ij} = (C_{ij})^{-1}$ ) of  $Mn_{15}Si_{26}$  has been deduced from these experimental measurements as well as calculated using Ab-initio calculations. The macroscopic elastic modulus (E, G, B) and Poisson's coefficient have been examined and discussed and their 3D-representation has been plotted. The mechanical anisotropy hereby evidenced as the existence of anisotropy of the thermoelectric properties could be a significant factor for the mechanical reliability of thermoelectric modules which consisted of  $Mn_{15}Si_{26}$  legs with a possible preferred crystallographic orientation induced during their fabrication.

## 1. Introduction

A thermoelectric module (TEM) is an electrical device which converts the thermal gradient into electrical energy through the Seebeck effect. It is an environmentally friendly energy conversion technology, which has drawn the attention of industries such as the automotive and aerospace ones, especially for waste-heat recovery applications [1–3]. The performance of thermoelectric materials is determined from the dimensionless figure of merit, defined as  $ZT = \frac{S^2 T}{\kappa \rho}$  (S: Seebeck coefficient, T: absolute temperature,  $\kappa$ : thermal conductivity, and  $\rho$ : electrical resistivity). In order to obtain

the highest figure of merit, a material with a large Seebeck coefficient, low thermal conductivity and high electrical conductivity is required [4,5]. On the other hand, these materials have to withstand the mechanical stresses they may be subject to during the manufacturing process as well as in service in order to ensure the long-term durability and reliability of the TEMs [6,7]. Consequently, the best mechanical properties are sought so as to prevent failures such as cracks and delamination within the materials ensuring the connections inside the TEM that may be subject to thermomechanical stresses resulting from the imposed thermal gradients [8,9]. For example, knowledge of the stiffness (elasticity) tensor is required as input data for the thermomechanical modeling of the behavior of TEMs. This same tensor is also needed in order to determine the radiocrystallographic elastic constants, which allow us to quantify the residual stresses of the constituent materials of the TEMs, which

\* Corresponding author.

E-mail address: [estournes@chimie.ups-tlse.fr](mailto:estournes@chimie.ups-tlse.fr) (C. Estournès).

might be responsible for the failure of the modules in service in the more or less long term.

$\text{MnSi}_\gamma$  ( $\gamma = 1.71 - 1.75$ ) compounds are a unique family of higher manganese silicide (HMS) materials with the highest silicon-rich intermediate phase in the Mn-Si binary phase diagram. Over the past 30 years, HMSs have undergone extensive studies due to their large Seebeck coefficient, low thermal conductivity and high electrical conductivity [5,10–18]. HMSs are suitable for medium temperature (500–800 K) heat sources such as automotive exhaust gases and industrial waste heat systems. HMSs present a ZT value of 0.3–0.4 at 800 K. They are classified among the materials which are eco-friendly, cheap p-type thermoelectric semiconductors with a high thermal stability thanks to their high melting point and good mechanical properties [7,19].

HMS phases crystallize in the tetragonal Nowotny chimney ladder structure, which is composed of the Mn and Si sub-lattices with similar lengths of the  $a$ -axes and rational  $c$ -axis sizes (see [Supplementary Material](#)) [20]. For  $1.71 \leq \gamma \leq 1.75$ , several structural formulas of HMSs with different lattice parameters, such as  $\text{Mn}_4\text{Si}_7$ ,  $\text{Mn}_{11}\text{Si}_{19}$ ,  $\text{Mn}_{15}\text{Si}_{26}$ , and  $\text{Mn}_{27}\text{Si}_{47}$  are known [10,21,22]. This difference between  $a$  and  $c$ -axis (( $\text{Mn}_4\text{Si}_7$ ,  $c/a \sim 3.16$ ) [23], ( $\text{Mn}_{15}\text{Si}_{26}$ ,  $c/a \sim 12$ ) [24]) results a strong anisotropy in the thermoelectric and magnetic properties of HMSs [25–27]. It was found that thermoelectric properties of HMSs in the [001] and [100] directions show anisotropy [28,29].

The microstructural properties and electrical performance of HMSs have been widely studied, but data on their mechanical properties are missing. Several studies have confirmed the impact of crystal orientation on the mechanical properties, especially in tetragonal systems, including Young's modulus and nanohardness, such as  $\text{KSr}_2\text{Nb}_5\text{O}_{15}$  [30],  $\text{TiAl}$  [31] and Zirconia [32]. As a consequence, the investigation of these properties is essential in expanding the field of applications for this material and in particular in order to increase the reliability of the TEMs.

Over the last three decades, nanoindentation has become an advanced technique used to investigate the plasticity, Young's modulus and nanohardness of several materials, such as ceramics, metals and thin films. The load and depth of the indenter are continuously recorded during a loading and unloading cycle. Analysis of the loading-unloading curve permits to calculate the Young's modulus of the samples by measuring the slope of the initial portion of the unloading curve and nanohardness by integrating the area under the curve [33].

In the present study, we investigate the elastic properties of  $\text{Mn}_{15}\text{Si}_{26}$  by performing experimental nanoindentation measurements. A study of this nature, to our knowledge have never been reported in the current literature for this type of material. In addition, we envisaged the coupling of such an analysis to the crystallographic orientation of the grains of the material determined by means of characterizations by electron backscattering diffraction (EBSD). This type of approach has not been reported yet. This should allow us to determine the stiffness tensor of  $\text{Mn}_{15}\text{Si}_{26}$ , which crystallizes in a tetragonal system. Consequently, mechanical properties such as Young's modulus, bulk modulus, shear modulus and Poisson's ratio will be determined and compared to Ab-initio calculations. The reported mechanical properties could be of particular interest in the field of thermoelectric packaging applications.

## 2. Materials and methods

### 2.1. Sintering and sample preparation

A sample of  $\text{MnSi}_\gamma$  ( $\gamma = 1.77$ ) powder with 99.99% purity and 20–50  $\mu\text{m}$  mean size was used. Dense cylindrical pellets, 60 mm in diameter and 5 mm thick, were fabricated using the spark plasma sintering (SPS) process by HotBlock Onboard. The SPS was

performed at 1130 °C with 5 min holding time and an applied uniaxial pressure of 50 MPa. These conditions have been optimized in previous studies [3,7]. For the EBSD and nanoindentation measurements, a smooth surface is required. After sintering, the density of the samples is measured using Archimedes' principle by means of a hydrostatic balance (Sartorius MSE22S-YDK03).

After mechanical polishing, the sample was then polished with a  $\frac{1}{4}$   $\mu\text{m}$  diamond polycrystalline suspension. In order to avoid a residual work-hardened surface, a 0.02  $\mu\text{m}$  colloidal silica suspension (OP-S) polishing was performed during one hour on a vibratory polishing machine, VibroMet 2 (Buehler). This final step is recommended to ensure a smoother and cleaner surface.

### 2.2. Structural and microstructural characterizations

The structures of the raw powder and the sintered samples were analyzed in transmission using a high-energy X-ray diffraction (HEXRD) on the P07 beamline at the Deutsches Elektronen Synchrotron (DESY, Hamburg, Germany). These measurements, performed with a 103 keV (0.119987 Å) monochromatic beam, allow for the analysis of the sample in its volume.

After metallographic preparation, EBSD analysis was conducted on a FEG-SEM (JEOL JSM-7100 F) equipped with an EBSD (Nordlys Nano). EBSD maps were acquired at an acceleration voltage of 20 kV, a beam current of about 10 nA and a working distance of 15 mm. Tango and Mambo softwares (HKL Channel5, Oxford Instruments) were used to determine phase distribution, grain orientation and pole figures. Large regions (400 × 400  $\mu\text{m}^2$ ) were studied with a fine step size (0.4  $\mu\text{m}$ ) in order to provide both local (grain orientation) and global (texture) information.

### 2.3. Nanoindentation

Following the EBSD analysis, nanoindentation tests were performed on selected grains with a CSM® Instruments UNHT nanoindenter equipped with a Berkovich tip and an optical microscope. Prior to the measurements, the cleaning and calibration of the indenter tip was performed on a silicon specimen. In this study, the maximum test force was set at 50 mN. The load was linearly applied with 60 s holding time of the full test load. In order to ensure the repeatability of the nanoindentation results, each grain was indented several times (more than 15 indents for the large grains). The nanoindentation tests were performed parallel to the normal surface of the selected grains and in the central part of the grains. The depth of the imprints ranged from 400 to 450 nm. The standard recommends a spacing of 20 times the indentation depth of the imprints [34]. The distance between imprints has been kept constant to 10  $\mu\text{m}$  (likewise from the grain boundary). This standard distance allowed us to rule out any interaction between the indentation-generated stress field and the elastic incompatibility stress field associated with the presence of the grain boundaries. The load and depth of the indenter were continuously monitored. Nanohardness and Young's modulus values were calculated according to the Oliver-Pharr method [33]. Nanohardness (Eq. (1)) is defined as a measure of the load-bearing capacity of the contact.

$$H = \frac{P_{\max}}{A} \quad (1)$$

With  $P_{\max}$  being the maximum load applied to the indenter and  $A$  the projected contact area.

The elastic contact stiffness,  $S$ , defined as the slope of the upper portion of the loading curve, is obtained directly from the load-displacement curve using Eq. (2).

$$S = \frac{dP}{dh} = \frac{2}{\sqrt{\pi}} E_r \sqrt{A} \quad (2)$$

With  $S$  being the slope of the discharge curve and  $E_r$  the reduced module.

The reduced module is defined by Eq. (3).

$$\frac{1}{E_r} = \frac{(1 - \nu^2)}{E} + \frac{(1 - \nu_i^2)}{E_i} \quad (3)$$

Where  $E$  and  $\nu$  are respectively Young's modulus and the Poisson coefficient of the material.  $E_i$  and  $\nu_i$  are respectively Young's modulus and the Poisson coefficient of the diamond indenter ( $E_i = 1141$  GPa and  $\nu_i = 0.07$ ).

#### 2.4. Density Functional Theory calculations

The  $Mn_{15}Si_{26}$  crystal structure has been built based on experimental crystallographic data. Density functional theory (DFT) calculations were performed using the Vienna *Ab-initio* calculations Package, VASP [35]. Calculations were carried out within the Perdew-Burke-Ernzerhof generalized gradient approximation of the exchange and correlation functional (PBE) [36] to the DFT [37,38]. Projector augmented wave (PAW) pseudo-potentials [39,40] were used, and a kinetic energy cut-off of 400 eV for the plane-wave basis set was adopted to compute energies. The  $k$ -mesh grids were sampled with  $\Gamma$ -centered  $8 \times 8 \times 1$  [41]. Magnetism was taken into account.

The elastic constants were computed using a stress-strain approach. In the case of the  $Mn_{15}Si_{26}$  system, two types of structure were considered: the primitive cell with 82 atoms and the conventional cell with 2 primitive cells. Details are provided in the Supplemental Material.

### 3. Results and discussion

#### 3.1. Structure and microstructure characterization

The HEXRD pattern of  $MnSi_i$  compound is shown in Fig. 1. The diffraction pattern was indexed using  $Mn_{15}Si_{26}$  (142d #122) (JCPDS No. 01-089-2413) and Si (Fm $\bar{3}m$  #225) (JCPDS No. 00-027-1402) [42]. The HEXRD pattern shows fine and intense peaks, which indicate a good crystallization of the sintered material with large crystallite sizes. After Rietveld refinement [43], the calculated lattice parameters of the  $Mn_{15}Si_{26}$  phase are  $a = b = 5.535(3)$  Å and  $c = 65.552(4)$  Å (Rwp ~ 7.3). The calculated lattice parameters are in good agreement with the reported standard XRD pattern of  $Mn_{15}Si_{26}$  (JCPDS No. 01-089-2413). Si fraction is  $2 \pm 1\%$ . The relative density of the  $MnSi_i$  compound measured by Archimedes' principle was 96%. The relative density was calculated using  $5.1 \text{ g/cm}^3$  as density for full dense material [3].

Fig. 2.a shows the band contrast, which reflects the quality of the EBSD patterns in gray levels (black = no or poor diffraction and white for very good diffraction) acquired on a polished surface of the  $MnSi_i$  sample. Si grains are presented in blue and grain boundaries with black lines (critical angle of  $10^\circ$ ). The  $Mn_{15}Si_{26}$  grain size diameter ranges from 2 to 67  $\mu\text{m}$ . Non-indexed pixels related to the presence of voids or polishing defects are in black. The 3D surface fraction of these voids, after considering the 2D corrective factor, was evaluated at 3.6% ( $2.6 \times 1.5$  [44]) by EBSD analysis. This value is slightly different from that expected from density measurements (i.e. 4%), probably due to image sampling effects.

Fig. 2.b (same area as Fig. 2.a), shows the inverse pole figure map (IPF Z) along the normal direction of the sample (Z-axis) with the selected grains of  $Mn_{15}Si_{26}$  phases on which the nanoindentation tests were carried out (G1 to G11, G1 for Grain1). Fig. 2.d shows the orientation of selected grains on the IPF. It covers various grain orientations, providing a suitable map for orientation dependence analysis of the mechanical properties. The 11 grains chosen with

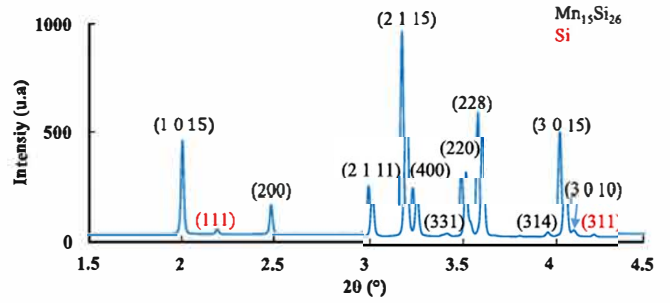


Fig. 1. The HEXRD pattern of  $MnSi_i$  after sintering.

different crystallographic orientations also have the advantage of having dimensions 10–15 times larger than the diagonal lengths of indentation ( $\sim 2 \mu\text{m}$ ).

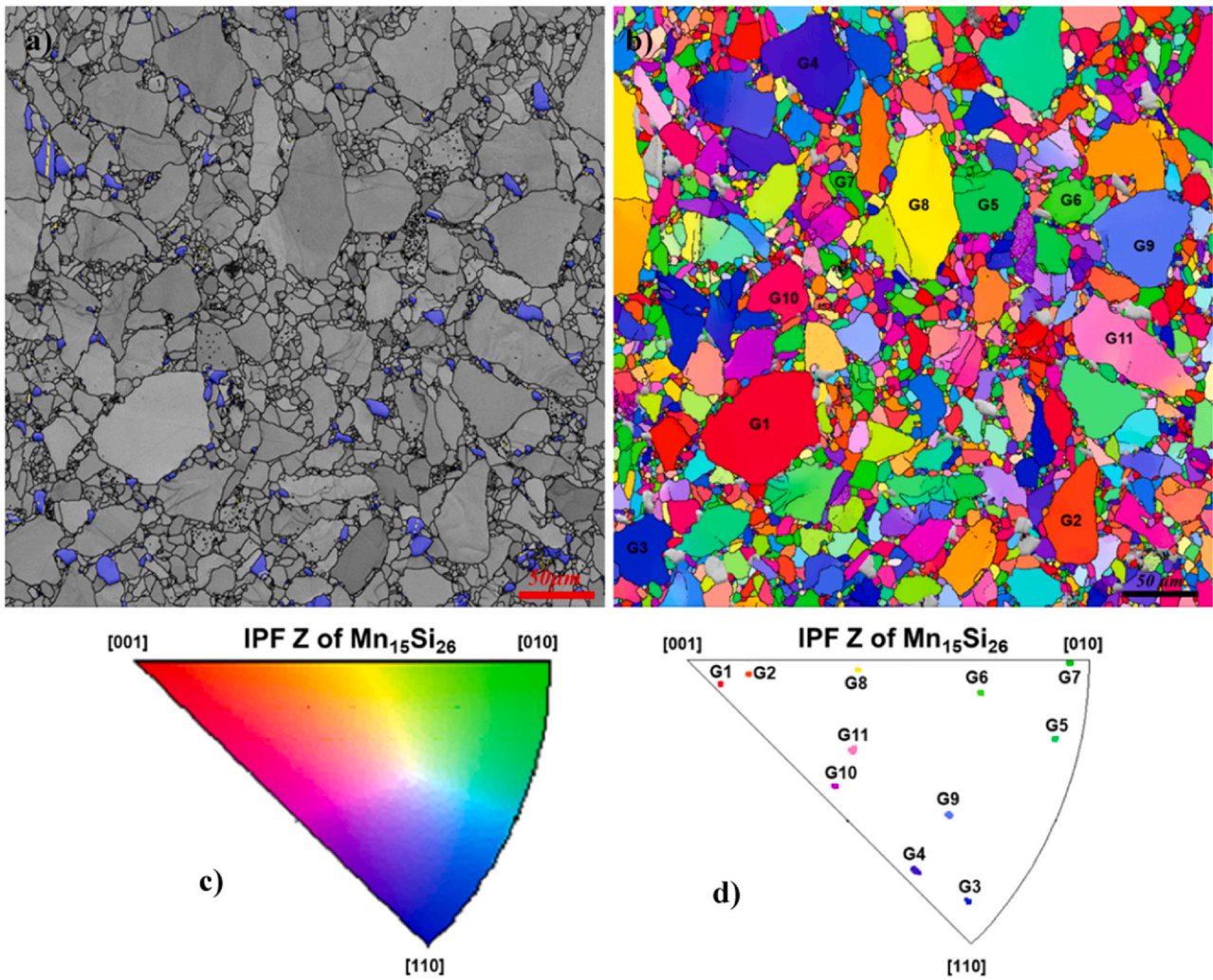
Fig. 3 presents the tetragonal pole figures in  $\langle 100 \rangle$ ,  $\langle 110 \rangle$ , and  $\langle 001 \rangle$  directions for the studied area on which the nanoindentation tests were performed. The color code corresponding to the multiple random orientations (mrd) i.e. for each specific orientation, the relative proportion between the numbers of grain analysed versus number of grains considering an isotropic distribution. With a maximum mrd close to 1 for the 2601  $Mn_{15}Si_{26}$  grains analysed on the map, we can consider there is no crystallographic texture in the HMS after sintering [45].

#### 3.2. Nanoindentation measurement analysis

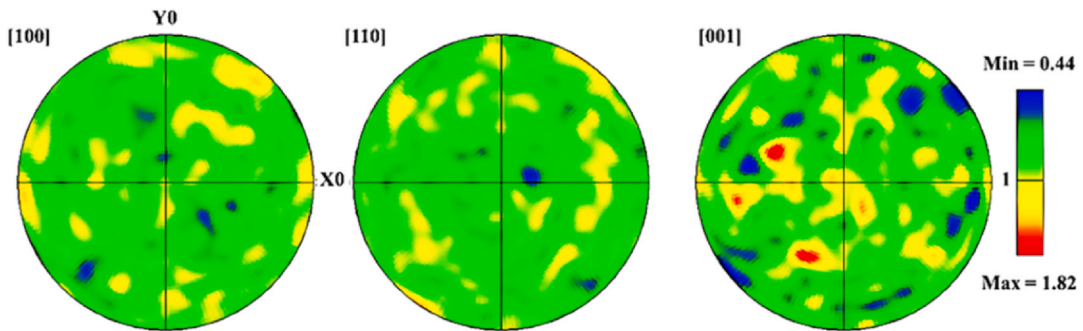
The influence of the grains' crystallographic orientation on the response of the  $Mn_{15}Si_{26}$  compound to nanoindentation testing was explored. Fig. 4 shows the arrangement of indents applied on grain 1 indexed in Fig. 2. These indents are typical and are selected to calculate the nanohardness and Young's modulus of differently oriented  $Mn_{15}Si_{26}$  grains after nanoindentation. To avoid any impact of the grain boundary on the mechanical properties measured, only the indents which were far enough from the grain boundary ( $\sim 10 \mu\text{m}$ ) were considered for the analysis [34].

Fig. 5 shows the typical loading-unloading curves, as observed during the nanoindentation test of  $Mn_{15}Si_{26}$ , with a normal indentation direction close to [001], [110] and [010] directions corresponding to grains 2, 3 and 7 respectively. Unloading is characterized by a slight shape recovery and significant residual deformation. It is to be noted that the response of the  $Mn_{15}Si_{26}$  material to nanoindentation with a Berkovich indenter depends on the crystallographic orientations of the grain. The load-displacement curve of grain 2 displays a higher unloading slope and the lowest indentation depths averaging 400 nm. On the other hand, the curve for grain 2 is more resistant ( $H \sim 20$  GPa) to the nanoindentation load than those of grains 3 and 7 ( $H \sim 16$  GPa). The maximum penetration ( $h_{\text{max}}$ ) in grains 3 and 7 (depth  $\sim 435$  nm) is larger than grain 2 (depth  $\sim 400$  nm).

The average values of Young's modulus and nanohardness of the different  $Mn_{15}Si_{26}$  grains selected and their crystallographic orientations (i.e. Euler angles) are summarized in Table 1. The number of indents per grain indicated in the last column is proportional to the surface of the grains. The higher average value of Young's modulus,  $300 \pm 16$  GPa, is obtained for grain 2 situated in the vicinity of the [001] crystallographic direction. The lowest value,  $234 \pm 10$  GPa, is obtained for grain 11 near the [12 12 1] direction. As Table 1 shows, the Young's modulus of the grains having a crystallographic orientation close to the [010] directions ( $244 \pm 7$  GPa) is lower than that of the grains having an orientation close to the [001] direction ( $290 \pm 9$  GPa), indicating that the elastic properties of  $Mn_{15}Si_{26}$  are anisotropic.



**Fig. 2.** (a) Band contrast map obtained on  $MnSi_7$  as sintered ( $Mn_{15}Si_{26}$ ). Si grains are presented in blue and grain boundaries as black lines. (b) EBSD Orientations map: inverse pole figure along the Z axis (IPF Z) which corresponds to the normal direction of the scanned area of  $Mn_{15}Si_{26}$  (without Si) with the numbering of grains measured by nanoindentation; (c) Corresponding IPF color code (standard triangle). (d) Position of the selected grains on IPF.



**Fig. 3.** Pole figures ([100]; [110]; [001]) of  $Mn_{15}Si_{26}$  for 2601 grains.

On the other hand, grain 2 presents the highest nanohardness value with a  $20.6 \pm 0.4$  GPa. Grain 3 presents the lowest nanohardness value with a  $16.3 \pm 0.4$  GPa. Just as for Young's modulus, anisotropy is observed in the case of nanohardness. The average nanohardness value for the 11 grains ( $18.5 \pm 0.5$  GPa) obtained by nanoindentation is higher than the Vickers nanohardness measured ( $16 \pm 1.1$  GPa, load of 0.1 kg for 10 s) that we have already reported [7]. This can be explained by the use of heavy loads (Vickers indentation) for indentation which favors the

generation of cracks (dissipated energy) which in turn reduce the nanohardness measured in the materials [7].

The anisotropy of the mechanical properties (E, H) according to the crystallographic orientation of the grains is confirmed. Thus, knowledge of the values of Young's modulus for various values of Euler angles should enable us to establish the stiffness tensor which, to the best of our knowledge, has never been reported in the literature so far.

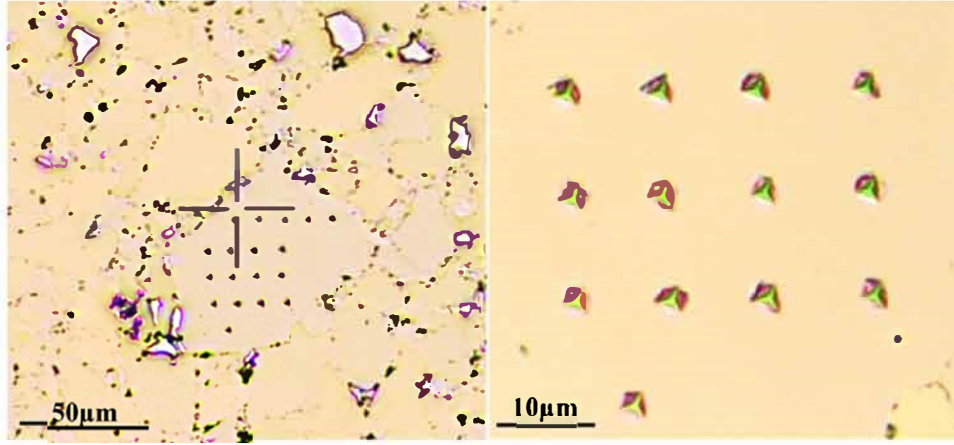


Fig. 4. The indentation marks on  $Mn_{15}Si_{26}$  for grain 1.

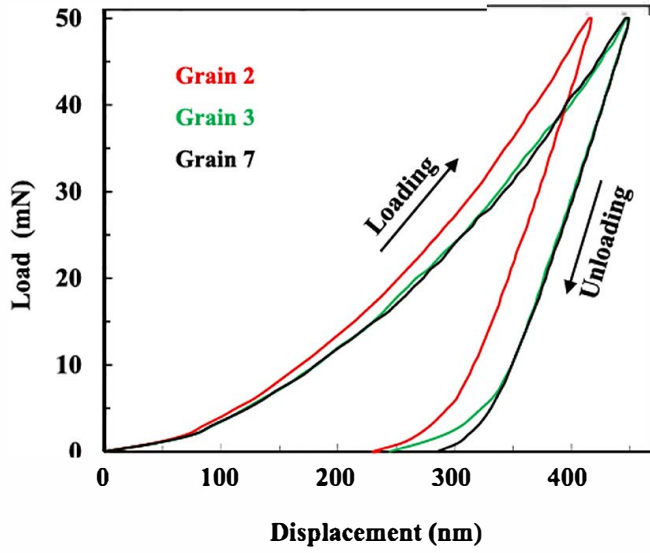


Fig. 5. Indentation loading-unloading curves for the  $Mn_{15}Si_{26}$  for grain 2, (close to [001]), 3 (close to [110]) and 7 (close to [010]) at 50 mN of maximum load.

**Table 1**  
The measured values (with standard deviation) of Young's modulus and nano-hardness of  $Mn_{15}Si_{26}$  in different crystallographic orientations.

Grain	Euler Angles		$E_{\phi_1 \psi}$		$H_{\phi_1 \psi}$		Nb of indents
	$\phi_1$	$\psi$	$\phi_2$ (GPa)	$\psi_2$ (GPa)	$\phi_2$ (GPa)	$\psi_2$ (GPa)	
1	167.9	168.3	1.6	290 ± 9	20.0 ± 0.7	16	
2	108.5	17.3	2.8	300 ± 16	20.6 ± 0.4	6	
3	8.7	85.4	5.4	243 ± 14	16.3 ± 0.4	9	
4	85.6	104.9	14.4	251 ± 7	16.8 ± 0.8	13	
5	8.4	93.9	5.4	244 ± 12	16.5 ± 0.6	9	
6	1.0	72.6	18.5	266 ± 10	18.8 ± 0.1	4	
7	18.6	87.1	2.6	244 ± 7	16.4 ± 0.1	3	
8	90.0	46.1	27.3	282 ± 15	19.3 ± 0.6	17	
9	7.0	105.8	15.6	267 ± 4	17.5 ± 0.4	16	
10	141.0	52.1	90.0	236 ± 11	17.6 ± 0.1	5	
11	70.0	129.8	27.7	234 ± 10	18.5 ± 0.7	15	

### 3.3. Stiffness tensor determination of $Mn_{15}Si_{26}$

The stiffness (elastic constants) tensor of the tetragonal structure has 6 independent components, and is represented by the square matrix (6×6) described in Eq. (4). It is described via the elastic constants expressed in Voigt notation as  $C_{ij}$ .

$$\bar{C} = \begin{pmatrix} C_{11} & C_{12} & C_{13} & 0 & 0 & 0 \\ C_{12} & C_{11} & C_{13} & 0 & 0 & 0 \\ C_{13} & C_{13} & C_{33} & 0 & 0 & 0 \\ 0 & 0 & 0 & C_{44} & 0 & 0 \\ 0 & 0 & 0 & 0 & C_{44} & 0 \\ 0 & 0 & 0 & 0 & 0 & C_{66} \end{pmatrix} \quad (4)$$

The mechanical stability criteria of a tetragonal structure are defined by expressions (5), (6), (7) and (8) [46].

$$\{C_{ii} > 0 \quad i = 1, 3, 4, 6\} \quad (5)$$

$$\{C_{11} - C_{12} > 0\} \quad (6)$$

$$\{C_{11} + C_{33} - 2C_{13} > 0\} \quad (7)$$

$$\{2(C_{11} + 2C_{12}) + C_{33} + 4C_{13} > 0\} \quad (8)$$

Considering the experimental values reported in the previous part, the stiffness tensor of  $Mn_{15}Si_{26}$  is calculated by correlating crystal orientations with the Young's modulus values obtained via nanoindentation measurements. Indeed, Young's modulus values for tetragonal structures can be calculated as the reciprocal of the compliance constants tensor ( $S_{ij}$ ) according to the expression (9) [30]. Both  $\alpha$  and  $\beta$  correspond to the tilt angle from the [001] direction and the rotation angle from [100] to [010] around the c-axis of the crystal, respectively.

$$\frac{1}{E_{\phi_1 \psi \phi_2}} = [S_{11}(\sin^4 \beta + \cos^4 \beta) + (2S_{12} + S_{66})\sin^2 \beta \cos^2 \beta]\sin^4 \alpha + (2S_{13} + S_{44})\sin^2 \alpha \cos^2 \alpha + S_{33} \cos^4 \alpha \quad (9)$$

$$\bar{S} = (\bar{C})^{-1} = \begin{pmatrix} S_{11} & S_{12} & S_{13} & 0 & 0 & 0 \\ S_{12} & S_{11} & S_{13} & 0 & 0 & 0 \\ S_{13} & S_{13} & S_{33} & 0 & 0 & 0 \\ 0 & 0 & 0 & S_{44} & 0 & 0 \\ 0 & 0 & 0 & 0 & S_{44} & 0 \\ 0 & 0 & 0 & 0 & 0 & S_{66} \end{pmatrix} \quad (10)$$

A Matlab code has been developed to estimate the stiffness tensor  $\bar{C}$  from the model (Eqs. (9) and (10)) and the Young's modulus measurements (Table 1). This code compiles all the data of the grains selected. The calculation is done by minimizing a least-square criterion on the Young's modulus values (squared error between the calculated (Eq. (9)) and nanoindentation measurements), with optimization variables set to the compliance constants tensor ( $S_{ij}$ ). These variables are constrained by nonlinear constraints (5), (6), (7), (8) and (10). Fig. 6.a and Fig. 6.b present the "parity graphs" between calculated and experimental Young's modulus. A quadratic

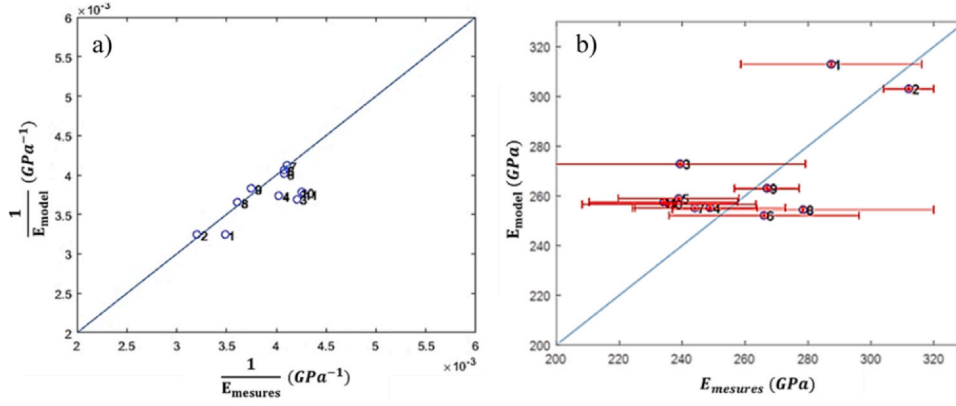


Fig. 6. Parity graph between calculated and experimental data, (a) inverse of Young's modulus and (b) Young's modulus.

standard deviation between the calculated and measured Young's modulus (for the 11 grains) is of the order of 20 GPa. Taking into account the measurement uncertainties for the Young's modulus measurement (error bar in Fig. 6), the model confirmed the available experimental data. The 'Bootstrap' method, which is a statistical inference method based on multiple data replication (1000 replications in our case) from the dataset studied, was used to determine the standard deviations of the  $C_{ij}$ .

Table 2 lists the elastic constants values and their standard deviations after calculation. An important difference of 21.5% (81 GPa) between  $C_{11}$  and  $C_{33}$  is noticed. This difference shows that the  $Mn_{15}Si_{26}$  phase presents a significant anisotropy in the mechanical properties. This is similar to the anisotropy of the thermoelectric properties of HMSs reported by Levinson et al. [28].

The elastic constants of  $Mn_{15}Si_{26}$  derived from ab-initio calculations were also listed in Table 2 (see details in the Supplemental Material). The latter clearly shows that the elastic constants derived from DFT calculations are in good agreement with the nanoindentation results. In terms of relative value, the  $S_{ij}$  values vary only by a maximum of 3% and the differences between  $C_{ij}$  (experimental and ab-initio calculations) range from 9% to 39%. Several factors may explain this difference. Firstly, the ab-initio calculations were performed on a perfect (i.e., defect-free) crystal structure, but (in reality) defects exist in the  $MnSi_v$  system. Secondly, since the  $MnSi_v$  material characterized is polycrystalline, the presence of grain boundaries may have an influence on the experimental results, yet they are not taken into account in the calculations. Thirdly, the position of the Mn and Si atoms (ordered/disordered structure) may have an influence on the calculated elastic constants [30].

The bulk modulus (B) represents the resistance to shape deformations under hydrostatic pressure. The shear modulus (G) describes the resistance to shear stress. Young's modulus (E) measures the uniaxial stress resistance. The bulk modulus (B) and the shear modulus (G) for a tetragonal structure can be calculated from the following expressions [47]:

For Reuss's theory (Eqs. 11–14),

$$G_R = 15 \left\{ \left( \frac{18B_R}{C^2} \right) + \left( \frac{6}{C_{11} - C_{12}} \right) + \left( \frac{6}{C_{44}} \right) + \left( \frac{3}{C_{66}} \right) \right\}^{-1} \quad (11)$$

Table 2. Experimental and calculated elastic constants of  $Mn_{15}Si_{26}$ .

Method	Indices ij	11	33	44	66	12	13
Experimental	$S_{ij}$ [ $10^{-3}$ GPa $^{-1}$ ]	3.9	3.1	10.3	8.5	-0.9	-0.8
	$C_{ij}$ [GPa]	296	377	97	117	88	102
DFT values	$S_{ij}$ [ $10^{-3}$ GPa $^{-1}$ ]	3.3	3.2	7.4	12.5	-0.8	0.6
	$C_{ij}$ [GPa]	337	344	135	107	96	80

$$B_R = \frac{C^2}{M} \quad (12)$$

$$C^2 = (C_{11} + C_{12})C_{33} - 2C_{13}^2 \quad (13)$$

$$M = C_{11} + C_{12} + 2C_{33} - 4C_{13} \quad (14)$$

For Voigt's theory (Eqs. 15 and 16),

$$B_V = \frac{1}{9} [2(C_{11} + C_{12}) + C_{33} + 4C_{13}] \quad (15)$$

$$G_V = \frac{1}{30} [M + 3(C_{11} - C_{12}) + 6(2C_{44} + C_{66})] \quad (16)$$

For Hill's approximation (Eqs. 17 and 18),

$$B_H = \frac{B_V + B_R}{2} \quad (17)$$

$$G_H = \frac{G_V + G_R}{2} \quad (18)$$

Young's modulus (E) and Poisson's ratio ( $\nu$ ) can thus be obtained from the bulk modulus and the shear modulus (Eqs. 19 and 20):

$$E = \frac{9 \cdot B \cdot G}{3 \cdot B + G} \quad (19)$$

$$\nu = \frac{3 \cdot B - 2G}{2(3B + G)} \quad (20)$$

Table 3 shows the obtained bulk modulus (B), Young's modulus (E), shear modulus (G) and Poisson's ratio ( $\nu$ ) of the tetragonal  $Mn_{15}Si_{26}$ . The macroscopic Young's modulus of  $Mn_{15}Si_{26}$  obtained with the Hill model is  $265 \pm 43$  GPa. The standard deviation on the Young's modulus value obtained by the Hill model was calculated by propagation from the standard deviations on the  $C_{ij}$ . The value is lower than the value measured by the frequency resonance method at 25 °C which was equal to  $281 \pm 2$  GPa [7]. The ductility and brittleness of the material depend on the value of Poisson's coefficient ( $\nu$ ) and the B/G ratio. High B/G values correlate with ductility and low values correlate with brittleness of the material. It was observed that the critical value of the transition from ductile to brittle behavior was about 1.75 [48]. The B/G ratios obtained ( $\sim 1.6$ ) are lower than 1.75, indicating the brittle nature of  $Mn_{15}Si_{26}$ .

Table 3. Calculated elastic properties of  $Mn_{15}Si_{26}$  via Voigt, Reuss and Hill models.

Model	B [GPa]	E [GPa]	G [GPa]	$\nu$
Voigt	172.6	266.7	107.3	0.242
Reuss	169.8	263.4	106.1	0.241
Hill	171.2	265	106.7	0.242



**Table 4**  
Minimum, maximum and anisotropy factor values of elastic properties  $Mn_{15}Si_{26}$ .

Proprieties	E [GPa]		$\beta$ [TPa <sup>-1</sup> ]		G [GPa]		$\nu$	
	$E_{min}$	$E_{max}$	$\beta_{min}$	$\beta_{max}$	$G_{min}$	$G_{max}$	$\nu_{min}$	$\nu_{max}$
Value	248.4	322.8	1.45	2.22	97	119	0.168	0.339
Anisotropy factor	1.3		1.53		1.23		2	

The Elate software was used to quantify anisotropic elastic properties, [49]. Table 4 shows the minimum, maximum and anisotropy factor values of Young's modulus (E), linear compressibility ( $\beta$ ), shear modulus (G) and Poisson's coefficient ( $\nu$ ). Table 4 displays a significant difference between the maximum and minimum values of each elastic property. Shear modulus has the lowest anisotropy value while Poisson's coefficient exhibits the highest value.

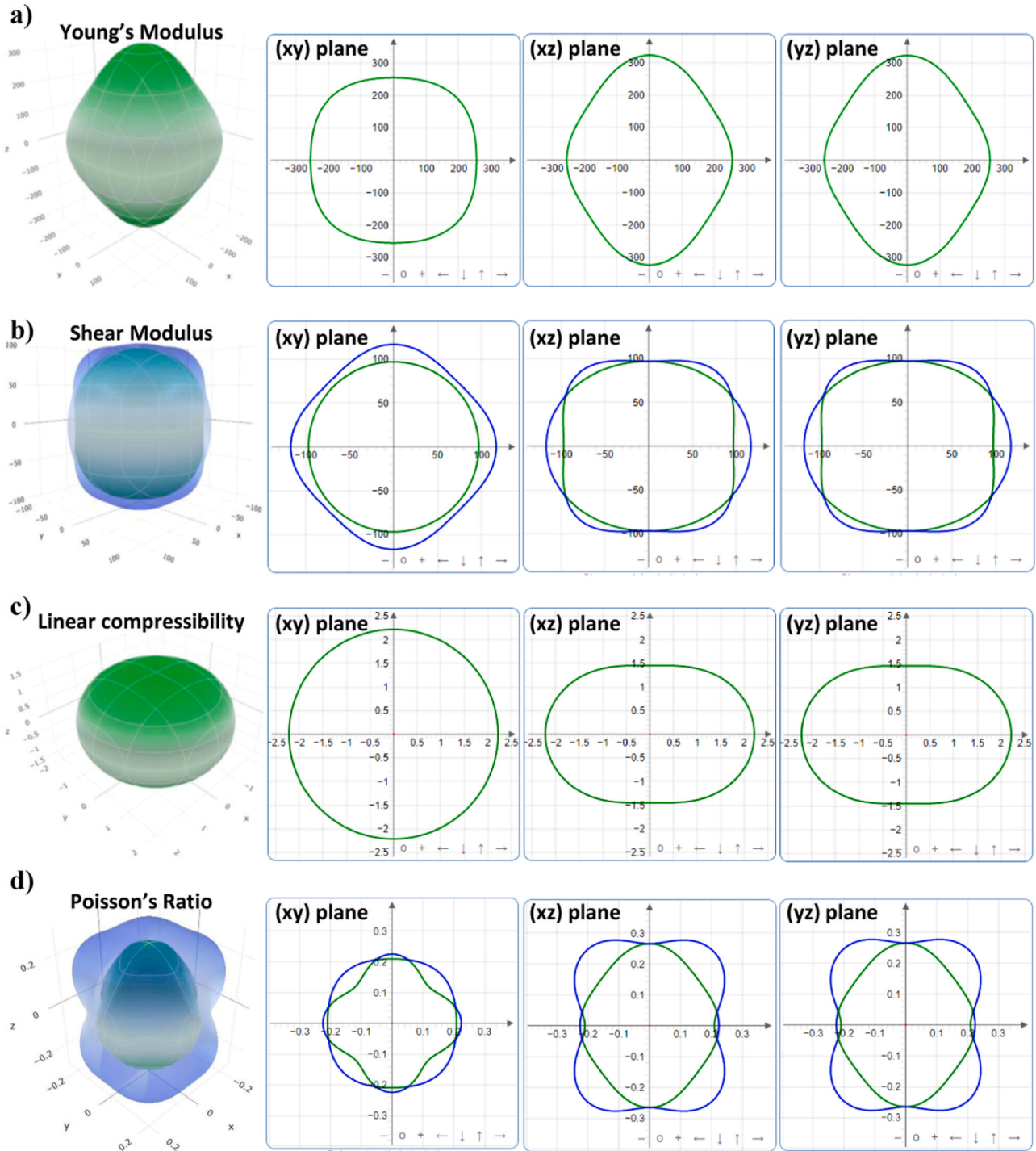


**Fig. 7.** The 3D and planer direction dependent on (a) Young's modulus (GPa), (b) shear modulus (GPa), (c) linear compressibility (GPa), and (d) Poisson's ratio of  $Mn_{15}Si_{26}$ . Maximum values displayed in blue and minimum values in green (shapes or curves).

The overall surface contours of Young's modulus, shear modulus, linear compressibility and Poisson's coefficient of  $\text{Mn}_{15}\text{Si}_{26}$  are reported in Fig. 7. The 3D-representation of elastic properties were plotted with the Elate software [49] which computed the experimental elastic constants. The planar projections in the [001] (xy-plane), [100] or (xz-plane) and [010] ((yz)-plane) crystallographic directions are also illustrated in Fig. 7. The spherical (or circular) shapes (or curves) indicate elastic isotropy. However, the distorted shapes (or curves) evidence elastic anisotropy. The green shapes (or curves) show the minimum values for the elastic properties and the blue ones show the maximum values. As detailed in Fig. 7, no spherical shapes are found for the different elastic properties plotted. For Young's modulus, shear modulus and Poisson's ratio, for the  $\text{Mn}_{15}\text{Si}_{26}$  compound, the x-axis (or y-axis) is more compressible than the z-axis. On the other hand, linear compressibility shows the opposite behavior.

#### 4. Conclusions

The structural, microstructural and mechanical properties of  $\text{Mn}_{15}\text{Si}_{26}$  have been examined by employing EBSD-nanoindentation coupling. EBSD analysis was used to provide a mapping of the crystallographic orientations of different grains of the  $\text{MnSi}_y$  compound. Subsequently, nanoindentation was deployed to explore the mechanical properties of several grains selected on the orientation maps. The experimental results reveal an average elastic modulus of 245 GPa and 295 GPa and an average nanohardness of 16 GPa and 20 GPa along the [010], [001] directions respectively. Nanohardness and Young's modulus of < 001 > orientations are higher than the < 100 > ones. Young's modulus of  $\text{Mn}_{15}\text{Si}_{26}$  in different crystallographic orientations revealed mechanical anisotropy.

The correlation of crystallographic orientations with the Young's modulus measured allowed for the calculation of the stiffness tensor of  $\text{Mn}_{15}\text{Si}_{26}$  using an appropriate model for a tetragonal system. The elastic constants of  $\text{Mn}_{15}\text{Si}_{26}$  fulfill the criteria for mechanical stability. Polycrystalline elastic properties (Young's modulus, shear modulus, bulk modulus) and anisotropy factors have been calculated via different models. For Hill calculations, the values of Young's modulus, shear modulus and bulk modulus are 265 GPa, 106.7 GPa and 171.2 GPa respectively. The anisotropy factor values of Young's modulus, shear modulus, linear compressibility and Poisson's ratio of  $\text{Mn}_{15}\text{Si}_{26}$  are 1.3, 1.23, 1.53 and 2 respectively. According to anisotropy factors and 3D surface construction, the elastic moduli of  $\text{Mn}_{15}\text{Si}_{26}$  are anisotropic.

On the other hand, elastic constants, derived from first-principles calculations, match with the experimental constants. Macroscopic Young's modulus (265 GPa) calculated from the stiffness tensor (extracted from nanoindentation measurements) is fairly consistent with the measured modulus values obtained via the frequency resonance method (281 GPa).

The stiffness tensor is required as input data for the mechanical modeling but also to determine the residual stresses of the different materials/interfaces constitutive of the TEMs based on the XRD patterns. This has been the subject of a separate study, which will be developed in a future article in order not to overload the present publication. These properties are essential in understanding the thermomechanical response of this material, and hence, in fabricating devices like thermometric modules that could provide predictable and long-term service. It is possible to manufacture a textured material and to promote orientation with high mechanical properties to ensure the reliability of the thermoelectric module.

#### CRediT authorship contribution statement

**M. Mejri:** Methodology, Investigation, Calculation, Validation, Writing - original draft., **B. Malard:** Methodology, Investigation,

Validation, Writing - review & editing, Supervision., **Y. Thimont:** Methodology, Investigation, Validation, Writing - review & editing., **P. Floquet:** Methodology, Investigation, Calculation, Writing - review & editing., **D. Connétable:** Methodology, Investigation, DFT calculation, Writing - review & editing., **R. Laloo:** Methodology, Investigation, Validation, Writing - review & editing., **A. Proietti:** Methodology, Investigation, Validation, Writing - review & editing., **C. Estournès:** Methodology, Investigation, Validation, Writing - review & editing, Supervision Project administration.

#### Declaration of Competing Interest

The authors declare that they have no known competing financial interests or personal relationships that could have appeared to influence the work reported in this paper.

#### Acknowledgments

This project is funded by the French National Research Agency (-ANR- 16-CE05-001203).

Authors would like to thank the partners from the company HotBlock OnBoard for supplying the pellets of thermoelectric materials. In addition, they would also like to thank Dr Viviane Turq for the fruitful discussions, suggestions and technical assistance in nanoindentation measurements. This work was performed using HPC resources from CALMIP (Grant 2020-p0912). The authors gratefully acknowledge the Deutsches Elektronen-Synchrotron (DESY-Petra III, Hamburg, Germany) for provision of beamtime at the PETRA P07-EH2 beamline. We would like to thank Olof Gutowski for his assistance during the experiment. The research leading to these results has been supported by the project CALIPSOplus under the Grant Agreement 730872 from the EU Framework Programme for Research and Innovation HORIZON 2020.

#### Appendix A. Supporting information

Supplementary data associated with this article can be found in the online version at doi:10.1016/j.jallcom.2021.163458.

#### References

- [1] S. Twaha, J. Zhu, Y. Yan, B. Li, A comprehensive review of thermoelectric technology: materials, applications, modelling and performance improvement, *Renew. Sustain. Energy Rev.* 65 (2016) 698–726, <https://doi.org/10.1016/j.rser.2016.07.034>
- [2] X.-L. Shi, J. Zou, Z.-G. Chen, Advanced thermoelectric design: from materials and structures to devices, *Chem. Rev.* 120 (2020) 7399–7515, <https://doi.org/10.1021/acs.chemrev.0c00026>
- [3] H. Ihou Mouko, K. Romanjek, M. Mejri, M. Oulfarsi, S. El Oualid, P. Malinconi, Y. Thimont, B. Malard, C. Estournès, N. David, A. Dauscher, Manufacturing and performances of silicide-based thermoelectric modules, *Energy Convers. Manag.* 242 (2021) 114304, <https://doi.org/10.1016/j.enconman.2021.114304>
- [4] D.M. Rowe, *Thermoelectrics Handbook: Macro to Nano*, CRC Press, 2018, <https://doi.org/10.1201/9781420038903>
- [5] X. She, X. Su, H. Du, T. Liang, G. Zheng, Y. Yan, R. Akram, C. Uher, X. Tang, High thermoelectric performance of higher manganese silicides prepared by ultrafast thermal explosion, *J. Mater. Chem. C* 3 (2015) 12116–12122, <https://doi.org/10.1039/C5TC02837J>
- [6] M. Mejri, B. Malard, Y. Thimont, K. Romanjek, H. Ihou Mouko, C. Estournès, Thermal stability of  $\text{Mg}_2\text{Si}_{0.55}\text{Sn}_{0.45}$  for thermoelectric applications, *J. Alloy. Compd.* 846 (2020) 156413, <https://doi.org/10.1016/j.jallcom.2020.156413>
- [7] M. Mejri, Y. Thimont, B. Malard, C. Estournès, Characterization of the thermomechanical properties of p-type ( $\text{MnSi}_{1.77}$ ) and n-type ( $\text{Mg}_2\text{Si}_{0.6}\text{Sn}_{0.4}$ ) thermoelectric materials, *Scr. Mater.* 172 (2019) 28–32, <https://doi.org/10.1016/j.scriptamat.2019.06.037>
- [8] J. Yin, Z. Liang, J.D. van Wyk, High temperature embedded SiC chip module (ECM) for power electronics applications, *IEEE Trans. Power Electron.* 22 (2007) 392–398, <https://doi.org/10.1109/TPEL.2006.889901>
- [9] Huazhong University of Science and Technology, C. Chen, A Review of SiC Power Module Packaging: Layout, Material System and Integration, *CPSS TPEA.* 2 (2017) 170–186, <https://doi.org/10.24295/CPSS TPEA.2017.00017>
- [10] Z. Li, J.-F. Dong, F.-H. Sun, S. Hirono, J.-F. Li, Significant enhancement of the thermoelectric performance of higher manganese silicide by incorporating MnTe

- nanophase derived from Te nanowire, *Chem. Mater.* 29 (2017) 7378–7389, <https://doi.org/10.1021/acs.chemmater.7b02270>
- [11] W. Luo, H. Li, Y. Yan, Z. Lin, X. Tang, Q. Zhang, C. Uher, Rapid synthesis of high thermoelectric performance higher manganese silicide with in-situ formed nano-phase of MnSi, *Intermetallics* 19 (2011) 404–408, <https://doi.org/10.1016/j.intermet.2010.11.008>
- [12] D.Y. Nhi Truong, D. Berthebaud, F. Gascoin, H. Kleinke, Molybdenum, tungsten, and aluminium substitution for enhancement of the thermoelectric performance of higher manganese silicides, *J. Electron. Mater.* 44 (2015) 3603–3611, <https://doi.org/10.1007/s11664-015-3854-x>
- [13] A. Nozariasbmarz, A. Agarwal, Z.A. Coutant, M.J. Hall, J. Liu, R. Liu, A. Malhotra, P. Norouzzadeh, M.C. Öztürk, V.P. Ramesh, Y. Sargolzaeiaval, F. Suarez, D. Vashaee, Thermoelectric silicides: a review, *Jpn. J. Appl. Phys.* 56 (2017) 05DA04, <https://doi.org/10.7567/JJAP.56.05DA04>
- [14] V. Ponnambalam, D.T. Morelli, S. Bhattacharya, T.M. Tritt, The role of simultaneous substitution of Cr and Ru on the thermoelectric properties of defect manganese silicides MnSi<sub>δ</sub> (1.73 < δ < 1.75), *J. Alloy. Compd.* 580 (2013) 598–603, <https://doi.org/10.1016/j.jallcom.2013.07.136>
- [15] M. Saleemi, A. Famengo, S. Fiameni, S. Boldrini, S. Battiston, M. Johnsson, M. Muhammed, M.S. Toprak, Thermoelectric performance of higher manganese silicide nanocomposites, *J. Alloy. Compd.* 619 (2015) 31–37, <https://doi.org/10.1016/j.jallcom.2014.09.016>
- [16] D.-K. Shin, K.-W. Jang, S.-C. Ur, I.-H. Kim, Thermoelectric properties of higher manganese silicides prepared by mechanical alloying and hot pressing, *J. Electron. Mater.* 42 (2013) 1756–1761, <https://doi.org/10.1007/s11664-012-2415-9>
- [17] Y. Thimont, L. Presmanes, V. Baylac, P. Tailhades, D. Berthebaud, F. Gascoin, Thermoelectric Higher Manganese Silicide: Synthesized, sintered and shaped simultaneously by selective laser sintering/Melting additive manufacturing technique, *Mater. Lett.* 214 (2018) 236–239, <https://doi.org/10.1016/j.matlet.2017.12.026>
- [18] A. Yamamoto, S. Ghodke, H. Miyazaki, M. Inukai, Y. Nishino, M. Matsunami, T. Takeuchi, Thermoelectric properties of supersaturated Re solid solution of higher manganese silicides, *Jpn. J. Appl. Phys.* 55 (2016) 020301, <https://doi.org/10.7567/JJAP.55.020301>
- [19] Y. Gelbstein, J. Tunbridge, R. Dixon, M.J. Reece, H. Ning, R. Gilchrist, R. Summers, I. Agote, M.A. Lagos, K. Simpson, C. Rouaud, P. Feulner, S. Rivera, R. Torrecillas, M. Husband, J. Crossley, I. Robinson, Physical, mechanical, and structural properties of highly efficient nanostructured n- and p-silicides for practical thermoelectric applications, *J. Electron. Mater.* 43 (2014) 1703–1711, <https://doi.org/10.1007/s11664-013-2848-9>
- [20] Y. Miyazaki, D. Igarashi, K. Hayashi, T. Kajitani, K. Yubuta, Modulated crystal structure of chimney-ladder higher manganese silicides MnSi<sub>γ</sub> (γ ~ 1.74), *Phys. Rev. B* 78 (2008), <https://doi.org/10.1103/PhysRevB.78.214104>
- [21] Z.-Q. Zou, W.-C. Li, J.-M. Liang, D. Wang, Self-organized growth of higher manganese silicide nanowires on Si(111), (110) and (001) surfaces, *Acta Mater.* 59 (2011) 7473–7479, <https://doi.org/10.1016/j.actamat.2011.08.050>
- [22] Y. Miyazaki, Y. Kikuchi, Higher manganese silicide, MnSi<sub>γ</sub>, in: K. Koumoto, T. Mori (Eds.), *Thermoelectric Nanomaterials*, Springer Berlin Heidelberg, Berlin, Heidelberg, 2013, pp. 141–156, [https://doi.org/10.1007/978-3-642-37537-8\\_7](https://doi.org/10.1007/978-3-642-37537-8_7)
- [23] O.G. Karpinskii, B.A. Evseev, Crystal Structure of the Compound Mn<sub>4</sub>Si<sub>7</sub>, in: A.N.N. Sirota (Ed.), *Chemical Bonds in Solids, Semiconductor Crystals, Glasses, and Liquids*, 4 Springer US, New York, NY, 1972, pp. 3–7 [https://doi.org/10.1007/978-1-4684-8682-7\\_1](https://doi.org/10.1007/978-1-4684-8682-7_1)
- [24] H.W. Knott, M.H. Mueller, L. Heaton, The crystal structure of Mn<sub>15</sub>Si<sub>26</sub>, *Acta Crystallogr.* 23 (1967) 549–555, <https://doi.org/10.1107/S0365110x67003184>
- [25] V.K. Zaitsev, Thermoelectric Properties of Anisotropic MnSi<sub><1.75></sub>, *CRC Handbook of Thermoelectrics*. (1995) 299–309.
- [26] I. Kawasumi, M. Sakata, I. Nishida, K. Masumoto, Crystal growth of manganese silicide, MnSi~1.73 and semiconducting properties of Mn<sub>15</sub>Si<sub>26</sub>, *J. Mater. Sci.* 16 (1981) 355–366, <https://doi.org/10.1007/BF00738624>
- [27] W.-D. Liu, Z.-G. Chen, J. Zou, Eco-friendly higher manganese silicide thermoelectric materials: progress and future challenges, *Adv. Energy Mater.* 8 (2018) 1800056, <https://doi.org/10.1002/aenm.201800056>
- [28] L.M. Levinson, Investigation of the defect manganese silicide Mn<sub>n</sub>Si<sub>2n-m</sub>, *J. Solid State Chem.* 6 (1973) 126–135, [https://doi.org/10.1016/0022-4596\(73\)90212-0](https://doi.org/10.1016/0022-4596(73)90212-0)
- [29] H. Kaga, Y. Kinemuchi, K. Watari, S. Tanaka, A. Makiya, Z. Kato, K. Uematsu, Fabrication of c-axis oriented higher manganese silicide by a high-magnetic-field and its thermoelectric properties, *J. Mater. Res.* 22 (2007) 2917–2923, <https://doi.org/10.1557/JMR.2007.0360>
- [30] Q. Chen, F. Gao, T. Csanádi, J. Xu, M. Fu, M. Wang, J. Dusza, Investigation of anisotropic mechanical properties of textured KSR<sub>2</sub>Nb<sub>5</sub>O<sub>15</sub> ceramics via ab-initio calculation and nanoindentation, *J. Am. Ceram. Soc.* 101 (2018) 5138–5150, <https://doi.org/10.1111/jace.15733>
- [31] Y. Wen, X. Zeng, Z. Hu, R. Peng, J. Sun, L. Song, A comparative first-principles study of tetragonal TiAl and Ti<sub>4</sub>Nb<sub>3</sub>Al<sub>9</sub> intermetallic compounds, *Intermetallics* 101 (2018) 72–80, <https://doi.org/10.1016/j.intermet.2018.07.012>
- [32] E.H. Kisi, C.J. Howard, Elastic constants of tetragonal zirconia measured by a new powder diffraction technique, *J. Am. Ceram. Soc.* 81 (1998) 1682–1684, <https://doi.org/10.1111/j.1151-2916.1998.tb02533.x>
- [33] W.C. Oliver, G.M. Pharr, An improved technique for determining hardness and elastic modulus using load and displacement sensing indentation experiments, *J. Mater. Res.* 7 (1992) 1564–1583, <https://doi.org/10.1557/JMR.1992.1564>
- [34] P. Sudharshan Phani, W.C. Oliver, A critical assessment of the effect of indentation spacing on the measurement of hardness and modulus using instrumented indentation testing, *Mater. Des.* 164 (2019) 107563, <https://doi.org/10.1016/j.matdes.2018.107563>
- [35] G. Kresse, J. Hafner, *Ab initio* molecular dynamics for liquid metals, *Phys. Rev. B* 47 (1993) 558–561, <https://doi.org/10.1103/PhysRevB.47.558>
- [36] J.P. Perdew, K. Burke, M. Ernzerhof, Generalized gradient approximation made simple, *Phys. Rev. Lett.* 77 (1996) 3865–3868, <https://doi.org/10.1103/PhysRevLett.77.3865>
- [37] P. Hohenberg, W. Kohn, Inhomogeneous electron gas, *Phys. Rev.* 136 (1964) B864–B871, <https://doi.org/10.1103/PhysRev.136.B864>
- [38] W. Kohn, L.J. Sham, Self-consistent equations including exchange and correlation effects, *Phys. Rev.* 140 (1965) A1133–A1138, <https://doi.org/10.1103/PhysRev.140.A1133>
- [39] P.E. Blöchl, Projector augmented-wave method, *Phys. Rev. B.* 50 (1994) 17953–17979, <https://doi.org/10.1103/PhysRevB.50.17953>
- [40] G. Kresse, J. Hafner, Norm-conserving and ultrasoft pseudopotentials for first-row and transition elements, *J. Phys. Condens. Matter* 6 (1994) 8245–8257, <https://doi.org/10.1088/0953-8984/6/40/015>
- [41] H.J. Monkhorst, J.D. Pack, Special points for Brillouin-zone integrations, *Phys. Rev. B* 13 (1976) 5188–5192, <https://doi.org/10.1103/PhysRevB.13.5188>
- [42] S. Gates-Rector, T. Blanton, The Powder Diffraction File: a quality materials characterization database, *Powder Diffr.* 34 (2019) 352–360, <https://doi.org/10.1017/S0885715619000812>
- [43] H.M. Rietveld, A profile refinement method for nuclear and magnetic structures, *J. Appl. Cryst.* 2 (1969) 65–71, <https://doi.org/10.1107/S0021889869006558>
- [44] M.I. Mendelson, Average grain size in polycrystalline ceramics, *J. Am. Ceram. Soc.* 52 (1969) 443–446, <https://doi.org/10.1111/j.1151-2916.1969.tb11975.x>
- [45] H.-J. Bunge, *Texture Analysis in Materials Science: Mathematical Methods*, Elsevier, 2013.
- [46] F. Mouhat, F.-X. Coudert, Necessary and sufficient elastic stability conditions in various crystal systems, *Phys. Rev. B* 90 (2014), <https://doi.org/10.1103/PhysRevB.90.224104>
- [47] Z. Huang, J. Feng, W. Pan, Theoretical investigations of the physical properties of zircon-type YVO<sub>4</sub>, *J. Solid State Chem.* 185 (2012) 42–48, <https://doi.org/10.1016/j.jssc.2011.10.050>
- [48] S.F. Pugh, XCII. Relations between the elastic moduli and the plastic properties of polycrystalline pure metals, *Lond. Edinb. Dublin Philos. Mag. J. Sci.* 45 (1954) 823–843, <https://doi.org/10.1080/14786440808520496>
- [49] R. Gaillac, P. Pullumbi, F.-X. Coudert, ELATE: an open-source online application for analysis and visualization of elastic tensors, *J. Phys. Condens. Matter* 28 (2016) 275201, <https://doi.org/10.1088/0953-8984/28/27/275201>

# Investigation of mechanical properties of $\text{Mn}_{15}\text{Si}_{26}$ via EBSD-nanoindentation coupling and *ab initio* calculation Supplement material

M. Mejri<sup>a</sup>, B. Malard<sup>b</sup>, Y. Thimont<sup>a</sup>, D. Connétable<sup>b</sup>, P. Floquet<sup>c</sup>,  
R. Laloo<sup>a</sup>, A. Proietti<sup>d</sup>, C. Estournès<sup>a,\*</sup>

<sup>a</sup> CIRIMAT, Université de Toulouse, CNRS, Université Toulouse 3 - Paul Sabatier, 118 Route de Narbonne, 31062 Toulouse cedex 9 - France

<sup>b</sup> CIRIMAT, Université de Toulouse, CNRS, INP- ENSIACET - 4 allée Emile Monso BP44362, 31030 Toulouse cedex 4 – France

<sup>c</sup> LGC, Université de Toulouse, CNRS, INP, UPS, Toulouse, France

Centre de Microcaractérisation Raimond Castaing, UMS 3623, Université de Toulouse, Espace <sup>d</sup> Clément Ader, 3 rue Caroline Aigle, 31400, Toulouse, France

\* Corresponding author: [estournes@chimie.ups-tlse.fr](mailto:estournes@chimie.ups-tlse.fr)

In this supplemental material, some results on three HSM systems,  $\text{Mn}_4\text{Si}_7$ ,  $\text{Mn}_{11}\text{Si}_{19}$ , and  $\text{Mn}_{15}\text{Si}_{26}$ , were presented: lattice parameters, magnetism and elastic properties of two of them for comparison.

## Methodology:

DFT calculations were performed using the Vienna *Ab initio* Simulation Package, VASP [1]. Simulations were carried out within the Perdew-Burke-Ernzerhof generalized gradient approximation of the exchange and correlation functional (PBE) [2] to the density functional theory [3,4]. Projector augmented wave (PAW) pseudo-potentials [5] were used, and a kinetic energy cut-off of 400 eV for the plane-wave basis set was adopted to compute energies. The  $\mathbf{k}$ -meshes grids were sampled with  $\Gamma$ -centered  $8 \times 8 \times 1$ . Magnetism was taking into account.

Elastic constants were computed using a stress-strain approach. In the case of the  $\text{Mn}_{15}\text{Si}_{26}$  system, two types of systems were used: either the primitive cell with 82 atoms or the conventional cell with 2 primitive cells.

Table 1: Lattice parameters ( $a_o$  and  $c_o$ , in Å), magnetism (in Bohr's magneton), space group and number of atoms per system.

Structure	Symmetry (space group)	Nb atom	$a_o$ [Å]	$c_o$ [Å]	$\mu_B$
Mn <sub>4</sub> Si <sub>7</sub>	P4c2 (116)	44	5.472/5.526 [6]	17.346/17.516 [6]	0
Mn <sub>11</sub> Si <sub>19</sub>	P4n2 (118)	120	5.486/5.518 [7]	47.681/48.136 [7]	2.0
Mn <sub>15</sub> Si <sub>26</sub>	I42d (122)	164	5.488/5.528 [8]/5.535 <sup>1</sup>	65.020/65.504 [8] 65.552 <sup>1</sup>	4.0
		82	5.496	64.866	2.0

## Results:

DFT results, see Table 1, show that the three HSM structures were well reproduced: lattice parameters are slightly smaller than experimental data, about 1% for  $a_o$  and  $c_o$ . Atomic positions are also in excellent agreement with measurements, as we can see in Table 2-3.

Mn<sub>4</sub>Si<sub>7</sub> is found semiconductor with a gap equal to 0.78eV, as found by Caprara *et al.*[9]. It is found to have any magnetism, in agreement with experimental findings [10]. Its dielectric tensor, calculated using the DFTP (cut-off energy equal to 500eV and with a 8x8x2 **k**-mesh), is slightly anisotropic:  $\epsilon_{11}=\epsilon_{22}=25.4$  and  $\epsilon_{33}=31.4$ .

Mn<sub>11</sub>Si<sub>19</sub> and Mn<sub>15</sub>Si<sub>26</sub> are found both metallic with a moment magnetic (about  $2\mu_B$  for the whole unit-cell), which is localized onto Mn atoms: for the Mn<sub>11</sub>Si<sub>19</sub> system present work is in agreement with Hammura *et al.* [10] for the Mn<sub>15</sub>Si<sub>26</sub> system see Ref. [11].

Table 1: Theoretical and experimental (in brackets) atomic positions in the Mn<sub>4</sub>Si<sub>7</sub> system [6].

atom	position	x	y	z
Mn	2a	0	0	1/4
Mn	2c	0	0	0
Mn	4i	0	0.5	0.0651 (0.0625)
Mn	4i	0	0.5	0.3082 (0.3125)
Mn	4h	0.5	0.5	0.1300 (0.125)
Si	8j	0.1589 (0.1627)	0.6788 (0.6791)	0.1825 (0.1815)
Si	8j	0.1993 (0.1933)	0.1554 (0.1507)	0.1128 (0.1129)
Si	8j	0.3461 (0.3436)	0.2302 (0.2279)	0.5388 (0.5409)
Si	4e	1/3	1/3	1/4

Table 2: Theoretical and experimental (in brackets) atomic positions in the Mn<sub>11</sub>Si<sub>19</sub> system [7].

atom	position	x	y	z
Mn	2a	0	0	0
Mn	4h	0	0.5	0.5236 (23/44=0.5227)
Mn	4e	0	0	0.4525 (20/44=0.4545)

Mn	4h	0	0.5	0.0697 (3/44=0.0682)
Mn	4e	0	0	0.0899 (4/44=0.0909)
Mn	4h	0	0.5	0.6114 (27/44=0.6136)
Mn	4e	0	0	0.3649 (16/44=0.3636)
Mn	4h	0	0.5	0.1588 (7/44=0.1590)
Mn	4e	0	0	0.1824 (8/44=0.1818)
Mn	4h	0	0.5	0.7062 (31/44=0.7045)
Mn	4e	0	0	0.2707 (12/44=0.2727)
Mn	2d	0	0.5	0.2501 (11/44=0.25)
Si	8i1	0.229 (0.237)	0.346 (0.340)	0.0142 (0.0132)
Si	8i2	0.845 (0.838)	0.195 (0.188)	0.0414 (0.0423)
Si	8i3	0.326 (0.331)	0.159 (0.171)	0.0666 (0.0673)
Si	8i4	0.669 (0.673)	0.338 (0.337)	0.0918 (0.0909)
Si	8i5	0.155 (0.168)	0.311 (0.315)	0.1168 (0.1173)
Si	8i6	0.782 (0.778)	0.153 (0.158)	0.1432 (0.1442)
Si	8i7	0.347 (0.342)	0.257 (0.268)	0.1716 (0.1710)
Si	8i8	0.795 (0.788)	0.346 (0.337)	0.1994 (0.1978)
Si	8i9	0.157 (0.161)	0.179 (0.183)	0.2250 (0.2262)
Si	4g	0.665 (0.671)	0.165 (0.171)	1/4

Table 3: Theoretical and experimental atomic positions in the  $Mn_{15}Si_{26}$  system [12].

atom	position	x	y	z
Mn	4a	0	0	0
Mn	8c	0	0	0.0662 (0.0653)
Mn	8c	0	0	0.1336 (0.1330)
Mn	8c	0	0	0.1988 (0.1996)
Mn	8c	0	0	0.2673 (0.2669)
Mn	8c	0	0	0.331 (0.3326)
Mn	8c	0	0	0.4011 (0.4013)
Mn	8c	0	0	0.4652 (0.4644)
Si	16e	0.2295 (0.2161)	0.3467 (0.3445)	0.0104 (0.0119)
Si	16e	0.8455 (0.8515)	0.1966 (0.1811)	0.030 (0.0311)
Si	16e	0.3249 (0.3167)	0.1590 (0.1642)	0.0488 (0.0480)
Si	16e	0.6680 (0.6657)	0.3373 (0.3434)	0.0670 (0.0680)
Si	16e	0.1563 (0.1591)	0.3152 (0.3122)	0.0853 (0.0848)
Si	16e	0.7883 (0.7744)	0.1534 (0.1523)	0.1044 (0.1063)
Si	8d	0.3464 (0.3479)	1/4	1/8

### Elastic properties:

As explained, one approach was used to compute elastic constants,  $C_{ij}$ : a strain-strain approach. In Table 5-6, results are summarized for the  $Mn_4Si_7$  and  $Mn_{15}Si_{26}$  systems, respectively.

Table 4:  $C_{ij}$  (in GPa) for the  $Mn_4Si_7$  system: bulk modulus: 195 GPa. Accuracy tested on this system with higher energy cut-off (500eV) and  $k$ -mesh grids ( $8 \times 8 \times 2$ ) without significant differences ( $< 2$  GPa).

375	114	99	0	0	0
114	375	99	0	0	0
99	99	373	0	0	0
0	0	0	143	0	0
0	0	0	0	143	0
0	0	0	0	0	114

Table 5:  $C_{ij}$  (in GPa) for the  $Mn_{15}Si_{26}$  system, bulk modulus 192 GPa with the conventional structure (162 atoms)

363	122	98	0	0	0
122	363	98	0	0	0
98	98	376	0	0	0
0	0	0	138	0	0
0	0	0	0	138	0
0	0	0	0	0	80

Table 6:  $C_{ij}$  (in GPa) for all structures. S-S= strain-stress method, S-E strain-energy method.

	Sym		$C_{11}$	$C_{33}$	$C_{44}$	$C_{66}$	$C_{12}$	$C_{13}$	$B_v$	$C_{11}+C_{12}$
$Mn_4Si_7$	tetral		375	373	143	114	114	99	195	489
$Mn_{15}Si_{26}$	tetral	$a_{theo}$	371/365	368	149	121	115	98	191	496
		$a_{exp}$	337	344	135	107	96	80	170	433

Two results were obtained: either using the theoretical lattice parameters (labeled  $a_{theo}$ ) or the experimental lattice parameters ( $a_{exp}$ ). The results show a slight decrease in  $C_{ij}$  when the experimental lattice parameters are used. This can be explained by the increase in bonds length and thus a softening of the interatomic links.

For both other system, i.e.  $Mn_4Si_7$  and  $Mn_{15}Si_{26}$  systems, results are strongly similar.

$$B_v = (2C_{11}+C_{33}+2C_{12}+4C_{13})/9$$

### Acknowledgments:

This work was performed using HPC resources from CALMIP (Grant 2020-p0912).

## Bibliography:

- [1] G. Kresse, J. Hafner, *Ab initio* molecular dynamics for liquid metals, *Physical Review B*. 47 (1993) 558–561. <https://doi.org/10.1103/PhysRevB.47.558>.
- [2] J.P. Perdew, K. Burke, M. Ernzerhof, Generalized Gradient Approximation Made Simple, *Phys. Rev. Lett.* 77 (1996) 3865–3868. <https://doi.org/10.1103/PhysRevLett.77.3865>.
- [3] P. Hohenberg, W. Kohn, Inhomogeneous Electron Gas, *Phys. Rev.* 136 (1964) B864–B871. <https://doi.org/10.1103/PhysRev.136.B864>.
- [4] W. Kohn, L.J. Sham, Self-Consistent Equations Including Exchange and Correlation Effects, *Phys. Rev.* 140 (1965) A1133–A1138. <https://doi.org/10.1103/PhysRev.140.A1133>.
- [5] G. Kresse, D. Joubert, From ultrasoft pseudopotentials to the projector augmented-wave method, *Physical Review B*. 59 (1999) 1758–1775. <https://doi.org/10.1103/PhysRevB.59.1758>.
- [6] U. Gottlieb, A. Sulpice, B. Lambert-Andron, O. Laborde, Magnetic properties of single crystalline Mn<sub>4</sub>Si<sub>7</sub>, *Journal of Alloys and Compounds*. 361 (2003) 13–18. [https://doi.org/10.1016/S0925-8388\(03\)00387-6](https://doi.org/10.1016/S0925-8388(03)00387-6).
- [7] Die Kristallstruktur von Mn<sub>11</sub>Si<sub>19</sub> und deren Zusammenhang mit Disilicid-Typen | SpringerLink, (n.d.). <https://link.springer.com/article/10.1007/BF00901708> (accessed January 14, 2021).
- [8] Thermal expansion studies of the group IV-VII transition-metal disilicides: *Journal of Applied Physics*: Vol 63, No 9, (n.d.). <https://aip.scitation.org/doi/abs/10.1063/1.340168> (accessed January 14, 2021).
- [9] S. Caprara, E. Kulatov, V.V. Tugushev, Half-metallic spin polarized electron states in the chimney-ladder higher manganese silicides MnSi<sub>1-x</sub> (x= 1.75– 1.73) with silicon vacancies, *The European Physical Journal B*. 85 (2012) 149.
- [10] K. Hammura, H. Uono, I.J. Ohsugi, T. Aono, E. De Ranieri, Magnetisation of bulk Mn<sub>11</sub>Si<sub>19</sub> and Mn<sub>4</sub>Si<sub>7</sub>, *Thin Solid Films*. 519 (2011) 8516–8519. <https://doi.org/10.1016/j.tsf.2011.05.041>.
- [11] S. Kang, G. Brewer, K.R. Sapkota, I.L. Pegg, J. Philip, Electrical and magnetic properties of higher manganese silicide nanostructures, *IEEE Transactions on Nanotechnology*. 11 (2011) 437–440.
- [12] H.W. Knott, M.H. Mueller, L. Heaton, The crystal structure of Mn<sub>15</sub>Si<sub>26</sub>, *Acta Crystallographica*. 23 (1967) 549–555. <https://doi.org/10.1107/S0365110X67003184>.